Multi-physics analysis and optimisation of high-speed train pantograph–catenary systems allowing for velocity skin effect

Xianrui Liu[1], Zefeng Yang[1], Song Xiao[1] ✉, Xuwei Duan[1], Guoqiang Gao[1], Wenfu Wei[1], Guangning Wu[1], Mihai Rotaru[2], Jan K. Sykulski[2]

[1]College of Electrical Engineering, Southwest Jiaotong University, Chengdu 611731, People's Republic of China
[2]Electronics and Computer Science, University of Southampton, Southampton SO17 1BJ, UK
✉ E-mail: xiaosong@home.swjtu.edu.cn

Abstract: A pantograph–catenary system (PCS) – an essential component to supply a high-speed train (HST) – faces a variety of new challenges due to the continuously increasing train speeds. The HST traction system receives power via an electrical contact between the pantograph strip and the high-voltage contact wire. This electrical contact is subject to serious mechanical shocks and significant electrochemical corrosion, making the modelling of the dynamic processes complicated, especially under high-speed and heavy-load conditions. The damage to the PCS – which is particularly noticeable at the edges of the pantograph strip – may become severe as the speed of the train rises. Moreover, as the speed increases, the distribution of the electrical current in the strip becomes uneven due to the velocity skin effect (VSE). To assess the impact of the VSE on the performance of PCSs, a multi-physics model has been created and is reported in this study. The model has been validated through experiments and the main aspects of its functionality – such as the VSE, friction, and air convection – have been identified and analysed at different speeds. The impact of speed on the traction current and the behaviour of thermal sources have been explored. With the increasing speed, the phenomenon of current clustering at the trailing edge of the strip becomes quite dramatic, resulting in a thermal surge in the region of the strip with high current density. To mitigate the negative impact caused by VSE in the PCSs, an improved kriging optimisation methodology has been utilised to optimise the parameters of the PCS. Recommendations regarding the optimal design of the PCS are put forward to improve the current-carrying performance and reduce the local temperature rise in the strip.

1 Introduction

The pantograph–catenary contact, fluid–structure interaction, and wheel–rail performance may be regarded as the three fundamental relationships for high-speed trains (HSTs), which determine their safety and reliability [1]. Being responsible for power transfer to HSTs, the pantograph–catenary system (PCS) plays a critical role in maintaining an uninterruptable and stable power supply for traction and control systems. The traction current is transferred from the overhead high-voltage catenary to the pantograph through

an electrical contact. Unlike normal electrical connections, the sliding contact between the pantograph strip and the overhead wire is exposed to serious mechanical shocks, substantial electrochemical corrosion, and generated high joule heat, especially under high-speed and heavy-load conditions. Moreover, because of the high maintenance cost of the catenary – and to protect the contact wire – the pantograph strips are designed as consumable components to abrade preferentially (Fig. 1).

The wear of the pantograph strip has always been of crucial concern in relation to the sliding electrical contact of the PCS. To understand the factors influencing the wear of the strip, research studies have analysed the effects of the sliding speed, contact force, electrical current, friction coefficient, and arc energy [2–4], while models for wear prediction have been constructed to describe the relationship between those factors [5]. With the drive to pursue higher and higher speeds, improvements to the structure and material of the pantograph strip are essential to satisfy the growing requirements in terms of the impact resistance, abrasion resistance, and electrochemical erosion resistance. The research has mainly focused on the sliding electrical contact of the PCS at low and medium speeds. Recently, the fastest HST named China Standard EMU (the electric multiple unit) was put into operation with a maximum speed reaching 350 km/h; the new generation of HSTs are expected to be even faster. As the speed of HST exceeds 350 km/h, new technical challenges emerge [6]. The increase of relative motion velocity exacerbates vibration and friction of the PCS, resulting in pantograph-catenary arcing [7] and severe ablation [8]. A test rig to simulate the sliding electrical contact of the PCS at speeds of 350 km/h [6] has been used, and it has been reported that although the upward tendency of the wear rate of the pantograph strip has further increased with the increasing speed, the upward tendency of arc energy has slowed down, while the friction coefficient has decreased. It has also been reported in [6] that the upward tendency of the temperature of the pantograph strip has
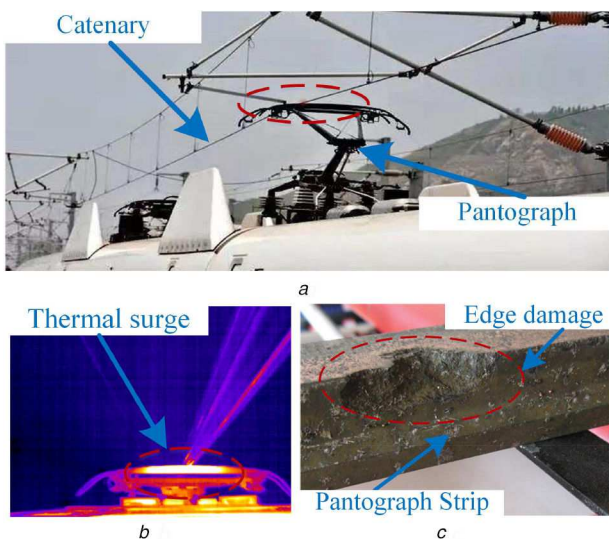

Fig. 1 *Thermal damage to the pantograph*
(a) A typical PCS, *(b)* Temperature distribution in the PCS, *(c)* The damage to the pantograph
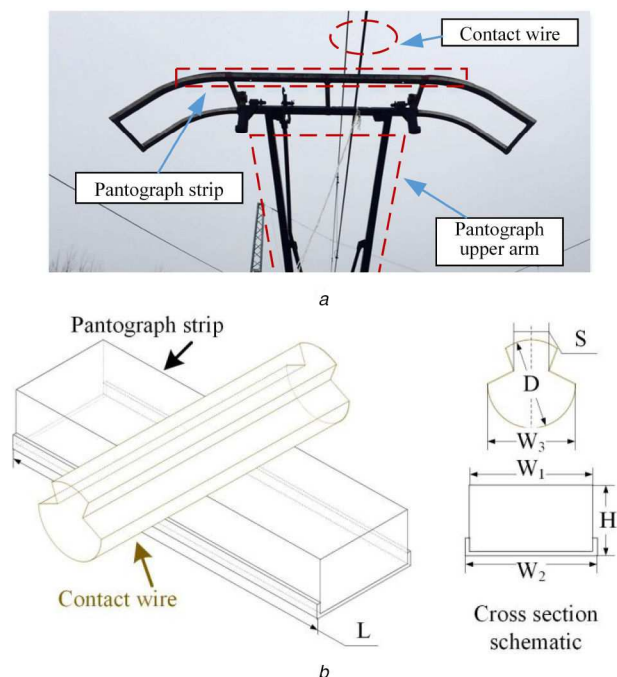
Fig. 2 *The PCS structure,*
(a) The layout of PCS, *(b)* The configuration of the PCS

Table 1 Geometrical parameters of the pantograph strip and contact wire

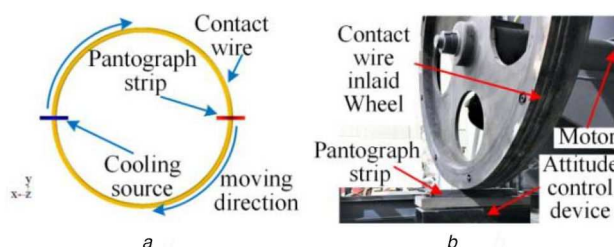| Structural parameters of the pantograph strip (CS0039)	Value	Structural parameters of the contact wire (CTMH-150)	Value
length L, mm	1030	normal area A, mm^2	150.0
head width W_1, mm	33.0	width W_3, mm	14.4
height H_1, mm	23.0	height H_2, mm	14.4
bottom width W_2, mm	35.0	groove spacing S, mm	6.8

Fig. 3 *The structures of the PCS model and device*
(a) The model of PCS, *(b)* Structure of the PCS experimental device

Table 2 Physical properties of the pantograph strip and contact wire

Section parameter	Carbon strip	Copper alloy wire
elastic modulus, GPa	12	126
density, kg mm^{-3}	2.4×10^3	8.9×10^3
conductivity, S m^{-1}	2.5×10^6	3.6×10^7
specific heat, J kg^{-1} K^{-1}	710	385
heat conductivity, W m^{-1} K^{-1}	150	400
emissivity	0.95	0.60
friction coefficient	0.2	

further increased with the increase of speed. Bearing in mind that the wear rate of the strip is positively related to its temperature [9], an analysis of the factors that can increase the temperature of the strip and thus further increase the wear of pantograph strip in addition to arc, vibration, and friction, appears to be crucial. As

speed increases, more traction power is needed to overcome air resistance; the convection process is affected, and traction current increases. Moreover, due to the motion between the pantograph strip and the catenary, a velocity skin effect (VSE) becomes pronounced [10, 11] and may become quite dramatic as the speed increases. The VSE is a phenomenon of current clustering observed in a region near the contact interface between two objects [12]. Owing to the VSE, the current tends to cluster at the trailing edge of the pantograph strip. The unevenly distributed current density inside the pantograph strip may directly lead to a local thermal surge. This local thermal surge at the trailing edge may trigger thermal damage in the region. Moreover, when pantograph strips pass under the rigid spots (the hitch points for hanging the contact wire) at high speed, the mechanical shock will exacerbate the damage, thus significantly reducing the efficiency and reliability of power transmission.

The damage to the pantograph is further aggravated by the already mentioned phenomenon of VSE, well known and thoroughly researched in the context of electromagnetic launchers, which has some similarities to the performance of PCSs, although the speeds here are not so high. Initially, VSE was observed as an asymmetric wear of recovered armatures [12]. Then, to explore its origins and properties, several VSE models were established for medium and low speeds [13, 14]. The characteristics of the VSE were found to be affected by several factors, such as armature geometry, material resistivity, and contact surface. A scheme for mitigating the current clustering phenomenon caused by VSE was also considered [15, 16]. The latest studies of VSE mainly focus on the multi-physics aspects, including vibration, gouging, transition, and melting erosion [17–20], which take place in EMLs at very high speeds.

Despite some similarities, there are also important differences between the operation of EMLs and PCSs; in the latter, the sliding electrical contact lasts a long time and the pantograph strip is continuously exposed to mechanical shocks, electrochemical corrosion, and high joule heat. The contact between the strip and the wire may be considered to be a line contact rather than a surface contact. To control the wear of the surface of the pantograph strip, the wire above the train body is arranged in a zigzag formation, thus the friction between the strip and contacting wire takes place not only in the direction of the train motion but also 'sideways'. In this study, the VSE in a PCS is examined. A multi-physics model – including electrical, magnetic, and thermal fields – has been created. Based on the model, the impact of the HST velocity on the traction current and other thermal sources can be assessed so that recommendations regarding the optimal design of the PCS may be put forward.

2 Modelling and verification

2.1 PCS model structure

The PCS configuration is shown in Fig. 2. The traction current from a substation is transmitted to the train through an electric contact from a 25 kV wire to the pantograph strip.

To facilitate the pursuit of higher speeds and larger traction power, advanced pantographs of higher electrical conductivity (e.g. Ti$_3$SiC$_2$/Cu) have been considered. Owing to a larger traction current, higher speed, and better conductivity of the pantograph strip, the VSE in the PCS can no longer be ignored. A model of the pantograph strip and contact wire has been established to describe induced currents [21–23]. The geometry parameters of the pantograph strip (Type number: CS0039) and contact wire (Type number: CTMH-150) are assumed as for the currently used systems as listed in Table 1 (the labels of parameters are consistent with the ones mentioned in Fig. 2*b*). The structure of the model and experimental setup for the PCS is presented in Fig. 3; the cooling source in Fig. 3*a* is used to maintain the contact wire at ambient temperature. Material properties of the pantograph strip and contact wire are listed in Table 2, with a friction coefficient of 0.2 selected based on experimental results.
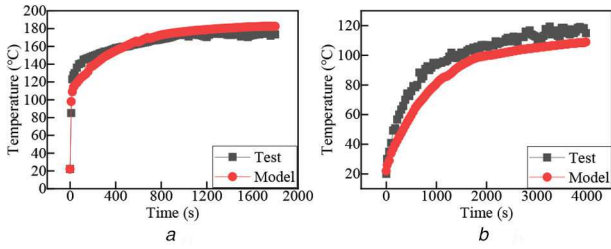
Fig. 4 *Comparison between test results and the model*
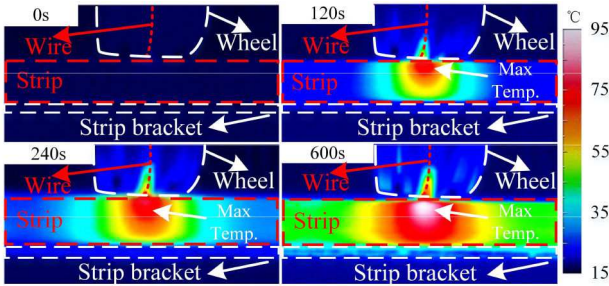*(a)* Velocity = 0 m/s, current = 100 A, *(b)* Velocity = 20 m/s, current = 100 A

Fig. 5 *Thermal image of the PCS test*

2.2 Magnetic effect

As mentioned before, with the rising operating speeds and increasing traction power, there is a requirement for advanced pantograph strips. Compared with original strips, which had poor conductivity ($<10^5$ S/m), the conductivity of advanced strips (10^6–10^7 S/m) is generally much higher. Consequently, the currents induced by the magnetic field of the PCS cannot be omitted [11], which is consistent with

$$\frac{\partial B}{\partial t} = \frac{1}{\mu \sigma_m} \nabla^2 B + \nabla \times (v \times B) \quad (1)$$

where B is the magnetic flux density, v is the velocity of HST, μ is the magnetic permeability, and σ_m is the electric conductivity of materials. Higher train speeds and increased currents both lead to a greater variation of the magnetic field.

2.3 Heat sources

Several heat sources contribute to temperature distribution within a PCS. The total heat Q_T includes Joule heat Q_J and friction Q_f, so that

$$Q_J = Q_T - Q_f = I^2 R_J = I^2 (R_V + R_c) \quad (2)$$

where the total equivalent resistance R_J is made up of the volume resistance R_V and contact resistance R_c, which in turn is the sum of a shrinkage resistance R_s and film resistance R_f [3, 24]. The film resistance may be ignored when relative motion takes place between the pantograph and the catenary; as a result, the contact resistance R_c is defined as

$$R_c \simeq R_s = (\rho_1 + \rho_2) / 4\alpha \quad (3)$$

where ρ_1 and ρ_2 are resistivities of the pantograph strip and contact wire, respectively, and α is the equivalent radius of the actual contact area. If the shape of the contact spot is assumed to be a circle, then the actual contact area of a rough surface is

$$A_r = F / n\xi H \quad (4)$$

where F is the pantograph-catenary contact force, n is the number of contact spots per unit area, ξ is the modification factor of elastic deformation, and H is the Brinell hardness of materials. Finally, the heat source related to friction is described by

$$Q_f = \mu_k F v \quad (5)$$

where μ_k is the friction coefficient of the PCS.

2.4 Heat diffusion

Cooling of the PCS is primarily achieved by convection at speeds of around or above 350 km/h. Following [25–27], the external forced convection Q_c is described by

$$Q_c = h_c(T_{atm} - T) \quad (6)$$

$$Q_r = \varepsilon\sigma(T_{atm} - T)^4 \quad (7)$$

where h_c is the externally forced convection coefficient (taking account of the shape of the strip), T_{atm} is the temperature of the airflow surrounding the HST, T is the surface temperature of the strip, ε is the surface emittance coefficient of materials, and σ is the Stefan-Boltzmann constant. Heat radiation effect Q_r is included above in (7).

2.5 Verification of the PCS model

To verify the effectiveness of the proposed model, tests using a PCS experimental platform (see Fig. 3) have been undertaken and the results are presented in Fig. 4. The thermal distributions locating on the strip's surface are observed by an infrared thermal imager (Type number: NEC InfRec R300 series) with the measuring range between 0 and 2000°C and with a temperature resolution as 0.05°C. Experiments at speeds of 0 and 20 m/s have been carried out with a test current of 100 A.

Comparison between experimental and modelling results reveals that the deviation of stabilised temperature is within 4%. It may therefore be argued that the model reflects with acceptable accuracy the thermal processes of a PCS at low speeds. The measurements were constrained by the limitation of the speed of the test device of 72 km/h. The temperature distributions around the strip's surface during the tests are presented in Fig. 5. Over time, the temperature rise in the strip is higher than the temperature rise in the contact wire, while the maximum temperature appears at the centre of the contact surface.

The current distribution of the PCS is affected by the VSE when the HST operates at 350 km/h; the velocity skin depth δ_V [28, 29] is defined by

$$\delta_v = k_e(4w / (\pi\sigma_m\mu v))^{1/2} \quad (8)$$

where k_e indicates the comparability between the saw tooth wave and the sine form current [28] (in our case $k_e = 1$), w is the interface length of the contact region (here the width of the pantograph strip), and v is the pantograph speed with respect to the catenary.

For the purpose of verification, a finite difference method (FDM) was also applied and the results compared with the analytical method and finite element simulations (FEMs). In the FDM model of the PCS, the pantograph strip was assumed to be stationary with the straight contact wire moving relative to this static strip. Otherwise, the remaining geometrical parameters in the FDM model were the same as for the FEM. Following (1), the magnetic diffusion equations governing the process in the contact wire and in the pantograph strip may be described as

$$\frac{\partial B}{\partial t} = \frac{1}{\mu\sigma_w}\left(\frac{\partial^2 B}{\partial x^2} + \frac{\partial^2 B}{\partial y^2}\right) - \frac{\partial B}{\partial x} \quad (9)$$

$$\frac{\partial B}{\partial t} = \frac{1}{\mu\sigma_s}\left(\frac{\partial^2 B}{\partial x^2} + \frac{\partial^2 B}{\partial y^2}\right) \quad (10)$$

where σ_w is the electric conductivity of the contact wire and σ_s is the electric conductivity of the pantograph strip. The boundary conditions suggested in [30] have been adapted here for the geometry of the PCS.
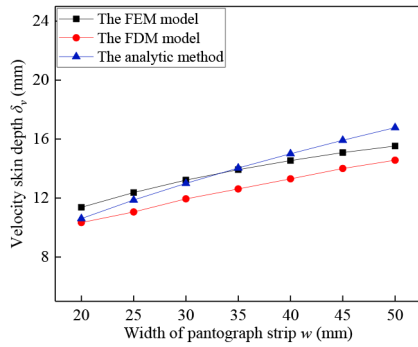
656

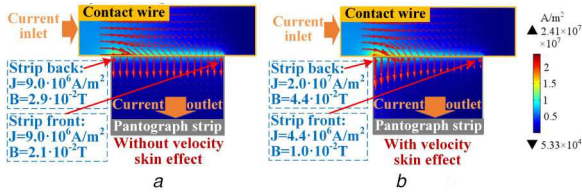**Fig. 6** *Analytic and modelling results of velocity skin depth in pantographs of different electrical conductivities*

Fig. 7 *Magnetic flux density and induced currents in the PCS*
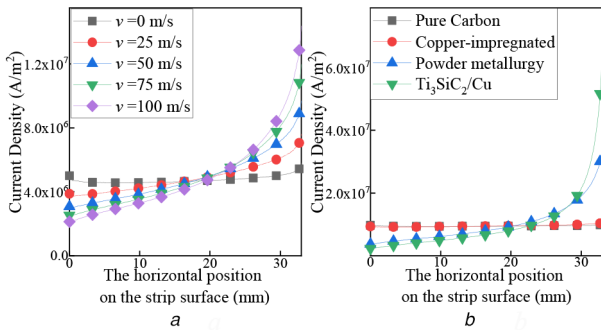*(a)* Without VSE, *(b)* With VSE

Fig. 8 *Current density on the surface of the pantograph strip taking account of the VSE*
(a) Varying speed, *(b)* Varying conductivity

Table 3 Different materials and the corresponding electric conductivity and velocity skin depth δ_v at 350 km/h

Material type	Pure carbon	Copper-impregnated metallised carbon	Powder metallurgy	Ti$_3$SiC$_2$/Cu
conductivity, 10^6 S/m	0.05	0.1	2.8	4.5
δ_v, mm	79	56	11	8.3

The uneven ratio of current r_δ

$$r_\delta = j_m \ / \ j_\delta \qquad (11)$$

is defined as the ratio of maximum current density j_m to current density at velocity skin depth j_δ on the contact surface of the pantograph strip, is utilised to evaluate the uneven current caused by VSE. The uneven ratio $r_\delta = e$ according to [29]. Assuming electric parameters of the PCS as in Table 2 and the speed of 350 km/h, several conditions with different widths of pantograph strips have been attempted by the analytical functions to observe the variation tendency of the velocity skin depth. Since the uneven ratio of current r_δ is the same at the velocity skin depth, the velocity skin depth can also be obtained by the PCS model. The results of δ_v obtained by the analytical method, the FDM model of PCS, and the FEM model of PCS are presented in Fig. 6.
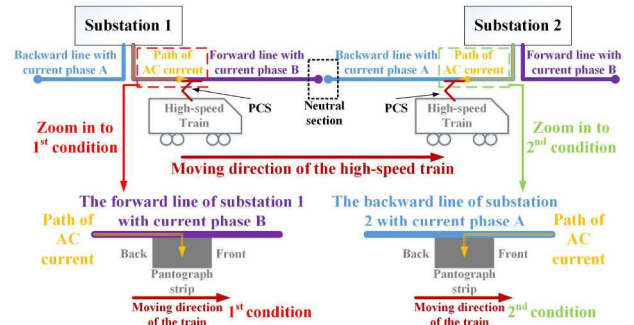

Fig. 9 *Train passing a substation*

Comparing the results obtained from the FEM model, FDM model and analytical equations, the deviation between the FEM model and analytic model is ~7.4% on average, while the deviation between the FEM model and FDM model is ~9.1%, which is considered to be acceptable.

3 Modelling results

The contact wire of a PCS is static, while the pantograph strip slides forward against the bottom of the wire. The current in the strip is affected by the magnetic field of the current in the wire. The sliding strip is exposed to a VSE; the consequences of such influence are depicted in Fig. 7, where the cases without and with the effect are shown for a Ti$_3$SiC$_2$/Cu strip (assuming current of 1 kA and speed of 350 km/h).

It can be seen that the VSE makes the current cluster at one side of the strip. The operating current is normally selected under the assumption of uniform current distribution, thus localised increases above such value will inevitably lead to undesirable thermal expansion effects and may accelerate the damage to the strip. Therefore, when pantograph strips have higher conductivity, the magnetic effects must not be neglected.

3.1 Velocity skin effect (VSE)

The speed of the train directly influences the VSE and consequently the current distribution. Assuming the traction current of 1 kA and strip conductivity of 2.5×10^6 S/m, the current density distributions along the width of the strip at different speeds are shown in Fig. 8a as a clear demonstration that the VSE becomes stronger with rising speed.

Conductivity also contributes to the VSE, although the current is hardly affected by the magnetic field in low conductivity materials, but strongly if conductivity is high, as seen in Fig. 8b, assuming electric parameters of four typical strip materials as in Table 3 and the speed of 350 km/h. Table 3 presents the velocity skin depth of different potential materials for the pantograph strips, which is calculated based on (8).

There is another, perhaps less obvious, influence related to the movement of the train in relation to the direction of the supply current. As the train moves along the track, it is supplied by one of the substations, either behind or in front, while passing by a substation also results in a change (from 'left line' to 'right line'), as explained by a simple sketch in Fig. 9. Thus, the pantograph strip either moves 'away' from the supply current or 'towards' it, as indicated at the bottom of Fig. 9; this results in two distinct conditions for the strip.

The effect is elucidated by the results of Fig. 10. The two distributions, on the left and on the right, may appear to be a mirror image, but in reality there is a noticeable difference in the actual values of both the flux density and, more importantly, the current density, as clearly marked in relevant boxes. Thus, when the train pulls away from the supplying substation the current density may be higher by as much as 10% compared with the case when it is moving towards a substation.
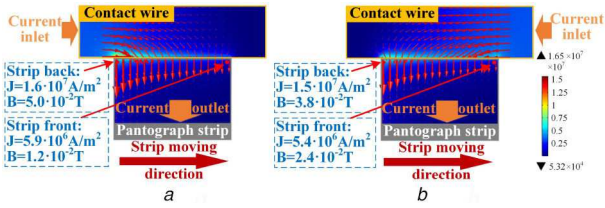
Fig. 10 *Cases of the train moving away and towards the supplying substations and related current density distributions*
(a) Moving away from the substations, *(b)* Moving towards the substations

Fig. 11 *Temperature distributions versus speed, strip conductivity, and wear of the contact wire*
(a) Velocity, *(b)* Strip conductivity, *(c)* Wear of the wire

Fig. 12 *Abrasion in the contact region of the wire*
(a) An intact wire, *(b)* A worn wire with abrasion

Table 4 Test setting of design parameters

		w_{strip}, mm	h_{strip}, mm	r_{wire}, mm
test	min	20.0	15.0	5.0
range	max	50.0	40.0	8.0
step size	—	0.1	0.1	0.02

3.2 Temperature distributions

The variation of the maximum strip temperature with the speed is shown in Fig. 11*a*, with the assumed traction current of 0.5 kA and the strip conductivity of 2.0×10^6 S/m. The temperature rises as the speed increases, and the strip endures higher temperatures at speeds above 350 km/h.

The variation of the maximum strip temperature with the strip conductivity is shown in Fig. 11*b*. Lower conductivity means larger volume and contact resistance of the strip, resulting in a sharp rise of the temperature. Consequently, manufacturers impose a rigid limit on current density to restrict the use of low conductivity strips; to obtain larger current capacity, high conductivity is necessary. With the increase of strip conductivity, the contribution of Joule heat loss to the temperature rise of the strip is noticeably reduced, thus the effects of friction and thermal dissipation of convection become dominant. However, higher conductivity results in enhanced VSE in the strip, causing a local increase of current density. Overall, due to the thermal effects of the contact resistance, the temperature of the contact area slightly increases.

The degree of wear of the surface of the contact wire also affects the temperature distribution in the pantograph strip. Compared with the strip, the contact wire has a longer service lifespan of 10–15 years. The bottom section of a new contact wire is arc-shaped, as shown in Fig. 12*a*. However, the contact wire is exposed to wear, gradually causing a flat bottom as in Fig. 12*b*; the contact area between a worn wire and the pantograph strip is slightly increased compared with the case of a brand new wire.

Accounting for the wear condition, the temperature distribution of the pantograph strip varies, as shown in Fig. 11*c*, ultimately causing a reduction of the maximum temperature of the pantograph strip.
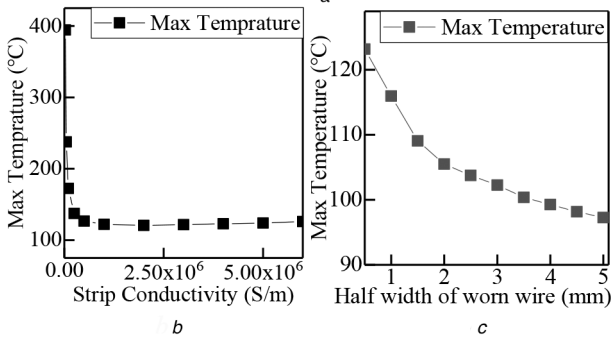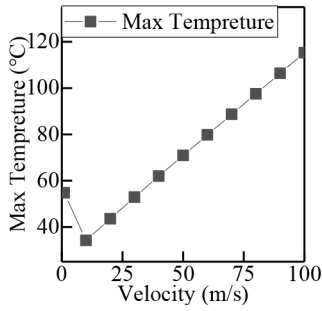
4 Multi-physics optimisation

4.1 Initialisation of the PCS structural optimisation

The wear of the pantograph strip and the resulting damage to the PCS are described in [7, 31] and are clearly aggravated as the speed of the train goes up, as explained before. The temperature rise may, however, be limited somewhat by careful choice of the shape and dimensions of the strip [32]; this observation gave the motivation to conduct proper optimisation of the PCS. Hence the focus of this stage of the study was to achieve some optimal parameters of the pantograph strip and the contact wire to improve the thermal dissipation performance. Many parameters can influence the maximum temperature and current distributions. After careful consideration, the following three were identified as the most important: the strip width w_{strip}, the thickness of the strip h_{strip}, and the cross-sectional radius of the contact wire r_{wire}, as shown in Table 4, while the remaining parameters were fixed as already given in Tables 1 and 2.

4.2 Objective functions

The thermal performance and current-carrying capability are the performance indices when designing pantograph strips. According to Fig. 11*b*, it can be found that the maximal temperature in the pantograph strip varies non-linearly with the unevenness ratio of current distribution. Hence when optimising the structure of pantograph strips, the design objectives of the optimisation problem need to involve the uneven ratio of current r_a [33] and surficial temperature of pantograph strip $T_{\max}$ separately. r_a is defined as the ratio of maximum current density j_m to average current density j_a on the contact surface of pantograph strip. The two objectives are defined as follows:

$$\begin{aligned} \text{Minimise } f_1(w_{\text{strip}}, h_{\text{strip}}, r_{\text{wire}}) &= r_a \\ \text{Minimise } f_2(w_{\text{strip}}, h_{\text{strip}}, r_{\text{wire}}) &= T_{\max} \end{aligned} \tag{12}$$

The initial values of the critical design variables are shown in Table 4, while the remaining parameters are fixed as shown in Table 2. To control the emphasis on these two objectives, a pair of weighting parameters is imposed on them. The objective function including two sub-objectives is defined as

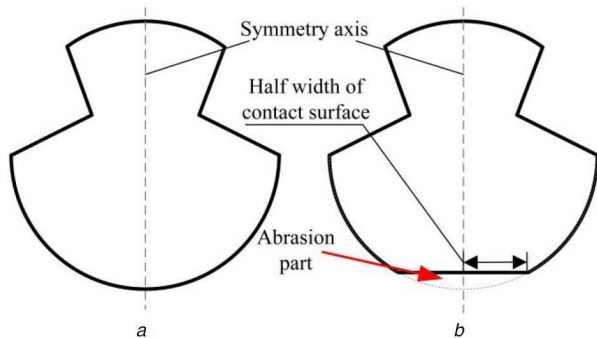$$\text{Minimise } f = w_1 \cdot f_1 + w_2 \cdot f_2 \tag{13}$$

4.3 Structural optimisation of pantograph strips

As a kind of regression model, kriging [34] is able to exploit the spatial correlation of data to predict the shape of the objective function and pursue the global optimum based on limited known information. Moreover, it can estimate the accuracy of this prediction throughout the iterative process, which may be very helpful in guiding the optimiser to locate the next evaluation point (vector). As the critical step in the kriging model, the correlation function is defined as follows (it relies on the linear regression model (13) and the Gaussian correlation model (14))

$$\hat{y}(x) = \sum_{k=1}^{m} \beta_k f_k(x) + \varepsilon(x) \qquad (14)$$

$$R\big(\varepsilon(x^i), \ \varepsilon(x^j)\big) = \prod_{k=1}^{m} e^{-\theta_k |x_k^i - x_k^j|^{p_k}} \qquad (15)$$

The sum $\sum_{k=1}^{m} \beta_k f_k(x)$ includes the linear combination of the values of initial sampled points x and may be viewed as a global approximation to the true function. The coefficients β_k are regression parameters, while ε is an additive Gaussian noise, representing the uncertainty. The model is statistical by assuming that the errors $\varepsilon(x^i)$ and $\varepsilon(x^j)$ are correlated. θ_k determines how fast the correlation between design vectors drops away in the kth coordinate direction, meanwhile p_k determines the function smoothness in the kth coordinate direction. The whole optimisation process made by the kriging surrogate model may be viewed as a Gaussian process γ, while a number of updating schemes can be adopted in this process. This allows the concept of improvement to be defined: for a single objective to be minimised, the improvement may be measured by comparing the value realised by the objective function with the current minimum of prediction, as presented below

$$I(x) = \max(f_{\min}) - \gamma(x) \qquad (16)$$

The expectation of improvement, which may also be called the expected improvement (EI) [35], is based on a potential error – the 'mean square error' produced by the kriging model – and is commonly used to select multiple designs for further evaluation.
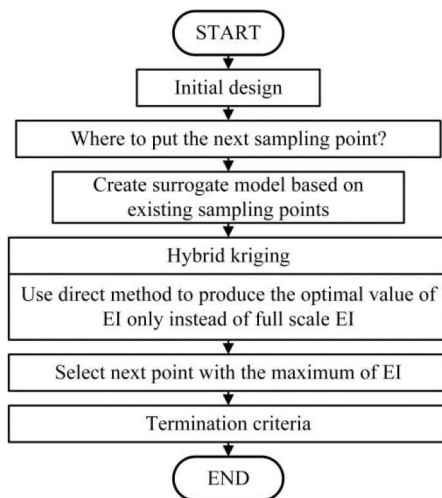

Fig. 13 *Decision-making chart for hybrid kriging (based on [37])*

Here the structural optimisation of pantograph strips may be viewed as minimising the objective function (13). The EI function is defined as

$$\mathrm{EIF}(x) =$$

$$\begin{cases} (f_{\min} - \hat{y}(x))\Phi\!\left(\dfrac{f_{\min} - \hat{y}(x)}{s(x)}\right) + s(x)\phi\!\left(\dfrac{f_{\min} - \hat{y}(x)}{s(x)}\right), & s(x) > 0 \\[2mm] 0, & s(x) = 0 \end{cases}$$
$$(17)$$

where $\hat{y}(x)$ is a value of the objective function predicted by kriging; $f_{\min}$ is the minimum value of y at the existed samples; $s(x)$ is the root mean square error produced by kriging; Φ and φ are the normal density and normal distribution functions, respectively. The maximum of EI indicates the position to select new sampling points when proceeding with iterations.

To reduce the computational cost of kriging in finding the next sampling point by constructing a full field EI over the whole design space based on very large correlation matrices, the kriging optimiser [36], developed previously, offers an effective methodology for searching a global optimum and was selected to perform this three-variable optimisation task. The 'direct optimisation' approach, motivated by a Lipschitzian algorithm, can address difficult global optimisation problems with constraints. The Lipschitzian optimisation process may be described as

$$|f(x) - f(x')| \le \alpha |x - x'| \ \forall \ x, \ x' \in M \qquad (18)$$

If the function f is Lipschitz continuous with a constant α, then this information can be utilised to seek the optimum of f iteratively. The optimisation algorithm used in this study is a hybrid kriging optimiser, which is a combination of the direct algorithm and kriging [37]. The optimising procedures for kriging and hybrid kriging are shown in Fig. 13.

The direct algorithm was used to assist kriging in selecting the next sampling point with an optimal value of EI, rather than building up a full-scale EI over the whole design space based on very large correlation matrices. The number of sampling points selected by kriging was increasing while the data produced by the EI remained almost constant.

4.4 Multi-objective optimisation

The optimisation goal of the pantograph-catenary structure contains two sub-objectives, which are minimising the uneven ratio of current distribution r_a and minimising the maximal temperature $T_{\max}$ appearing in the strips, when considering the impact brought from the Joule heat and friction heat. To adjust the balance between these two sub-objectives, two weighting parameters w_1 and w_2 are imposed on them based on (12) and (13). Some optimisation results with a different combination of weights are presented in Table 5.

When $w_1 = w_2 = 0.5$, the kriging optimiser required 429 calls of the FEM software before converging at the optimum solution ($w_{\mathrm{strip}} = 35.2$ mm, $h_{\mathrm{strip}} = 30.5$ mm, $r_{\mathrm{wire}} = 7.4$ mm), which provides the maximum temperature of 106.3°C, hence a noticeable improvement of 11.9% compared with the maximum temperature in a prototype, which was 120.7°C. The optimum solution above is to reduce the max temperature as much as possible while limiting the maximum current density. When $w_1 = 0.3$ and $w_2 = 0.7$, the best result in terms of the maximum temperature of the pantograph strip is achieved amongst the three cases. However, the best result

Table 5 Optimisation results of PCS with different weights combination

Weight	w_{strip}, mm	h_{strip}, mm	r_{wire}, mm	$T_{\max}$, °C	r_a	Max current density, 10^7 A m^{-2}
$w_1 = 0.3, w_2 = 0.7$	36.8	34.1	7.2	104.1	1.37	1.69
$w_1 = 0.5, w_2 = 0.5$	35.2	30.5	7.4	106.3	1.29	1.62
$w_1 = 0.7, w_2 = 0.3$	33.0	21.2	7.7	109.8	1.22	1.57

related to the current evenness is achieved when $w_1 = 0.7$ and $w_2 = 0.3$, which provides the max current density of 1.57×10^7 A/m^2, while the maximum current density in the prototype was 1.63×10^7 A/m^2. Therefore, in practice the weights on these two sub-objectives can be adjusted based on the preference of different performance requirements. Finally, to fully validate the thermal distribution of the PCS under the high-speed scenario, a field test will be developed, as the next step, to capture the VSE.

5 Conclusion

The PCS is a critical component for transmitting constant and stable power to HSTs. In contrast to stationary contacts, a sliding electric contact in a PCS experiences continuous mechanical shocks, arc erosion and high joule heat generation, especially under high-speed and heavy-load conditions. As the speed increases, the strips are prone to more damage, especially at the edges. The VSE phenomenon causes the electric current to cluster at the edges; this effect cannot be neglected at higher speeds and results in local thermal surges leading to thermal damage. To investigate the impact of VSE on the electrical contact of PCS, a multi-physics FEM model of the PCS has been built and its validity verified by a series of experiments and analytical models.

Pantograph strips made of different materials have been considered and their performance evaluated in the context of VSE. The relationship between the conductivity and the maximum temperature of the pantograph strip exhibits non-linearly. When the conductivity of the pantograph strip rises, the maximum temperature in the strip initially decreases due to the decreasing volume resistance; this is then followed by an increase in the temperature because of the current clustering in a local region. The optimal thermal performance of the pantograph strips of different conductivity was found at the inflection point of the maximum temperature in the strip.

Some parameters of the PCS have influence on the electrical and thermal performances. The VSE effect is mitigated somewhat when the width of the pantograph strip is increased. A thinner pantograph strip exhibits better thermal performance, but aggravates the VSE effect. The radius of the contact wire also influences the current distribution. However, the possibility of adjusting geometry parameters is constrained by many factors, such as fixed weight and aerodynamic performance.

Overall, because of the VSE, the current clusters and heat accumulates, therefore the quality of the electrical contact in the PCS deteriorates, thus accelerating the ageing and damage to the region near the strip edges. To alleviate these problems a kriging-assisted optimisation model has been developed to improve the current-carrying and thermal dissipation performance of pantograph strips.

6 Acknowledgments

7 References

[1] Zhang, W.H.: 'The development of China's high-speed railway systems and a study of the dynamics of coupled systems in high-speed trains', *Proc. Inst. Mech. Eng. F, J. Rail Rapid Transit*, 2014, **228**, (4), pp. 367–377

[2] Nituca, C.: 'Thermal analysis of electrical contacts from pantograph-catenary system for power supply of electric vehicles', *Electr. Power Syst. Res.*, 2013, **96**, pp. 211–217

[3] Plesca, A.: 'Thermal analysis of sliding electrical contacts with mechanical friction in steady state conditions', *Int. J. Therm. Sci.*, 2014, **84**, (1), pp. 125–133

[4] Giuseppe, B., Andrea, C.: 'A procedure for the wear prediction of collector strip and contact wire in pantograph-catenary system', *Wear*, 2009, **266**, (1), pp. 46–59

[5] Gao, S.B., Wang, Y., Liu, Z.G., *et al.*: 'Thermal distribution modeling and experimental verification of contact wire considering the lifting or dropping pantograph in electrified railway', *IEEE Trans. Transp. Electrific.*, 2016, **2**, (2), pp. 256–265

[6] Yang, H.J., Chen, G.X., Gao, G.Q., *et al.*: 'Experimental research on the friction and wear properties of a contact strip of a pantograph-catenary system at the sliding speed of 350 km/h with electric current'. the 20th Int. Wear of Materials Conf., Toronto, Canada, April 2015, pp. 949–955

[7] Wu, G.N., Zhou, Y., Gao, G.Q., *et al.*: 'Arc erosion of Cu-impregnated carbon materials used for current collection in high-speed railways', *IEEE Trans. Compon. Packag. Manuf. Technol.*, 2018, **8**, (6), pp. 1014–1023

[8] Yang, H.J., Hu, B., Liu, Y.H., *et al.*: 'Influence of reciprocating distance on the delamination wear of the carbon strip in pantograph–catenary system at high sliding-speed with strong electrical current', *Eng. Fail. Anal.*, 2019, **104**, pp. 887–897

[9] Nagasawa, H., Kato, K.: 'Wear mechanism of copper alloy wire sliding against iron-base strip under electric current', *Wear*, 1998, **216**, (2), pp. 179–183

[10] Lv, Q.A., Xiang, H.J., Lei, B., *et al.*: 'Physical principle and relevant restraining methods about velocity skin effect', *IEEE Trans. Plasma Sci.*, 2015, **43**, (5), pp. 1523–1530

[11] Engel, T.G., Neri, J.M., Veracka, M.J.: 'Characterization of the velocity skin effect in the surface layer of a railgun sliding contact', *IEEE Trans. Magn.*, 2008, **44**, (7), pp. 1837–1844

[12] Liebfried, O., Schneider, M., Stankevic, T., *et al.*: 'Velocity-induced current profiles inside the rails of an electric launcher', *IEEE Trans. Plasma Sci.*, 2013, **41**, (5), pp. 1520–1525

[13] Watt, T., Stefani, F.: 'The effect of current and speed on perimeter erosion in recovered armatures', *IEEE Trans. Magn.*, 2005, **41**, (1), pp. 448–452

[14] Hsieh, K.T., Stefani, F., Levinson, S.J.: 'Numerical modeling of the velocity skin effects: an investigation of issues affecting accuracy [in railguns]', *IEEE Trans. Magn.*, 2001, **37**, (1), pp. 416–420

[15] Uryukov, B.A.: 'The path of overcoming the velocity skin-effect in rail accelerators', *IEEE Trans. Magn.*, 2001, **37**, (1), pp. 466–469

[16] Stefani, F., Crawford, M., Melton, D., *et al.*: 'Experiments with armature contact claddings', *IEEE Trans. Magn.*, 2007, **43**, (1), pp. 413–417

[17] Che, Y.L., Yuan, W.Q., Xu, W.D., *et al.*: 'The influence of different constraints and pretightening force on vibration and stiffness in railgun', *IEEE Trans. Plasma Sci.*, 2017, **45**, (7), pp. 1154–1160

[18] Tang, B., Lin, Q.H., Li, B.M.: 'Research on thermal stress by current skin effect in a railgun', *IEEE Trans. Plasma Sci.*, 2017, **45**, (7), pp. 1689–1694

[19] Li, S.Z., Li, J., Xia, S.G., *et al.*: 'Phase division and critical point definition of electromagnetic railgun sliding contact state', *IEEE Trans. Plasma Sci.*, 2019, **47**, (5), pp. 2399–2403

[20] Li, C.X., Chen, L.X., Xia, S.G., *et al.*: 'Simulations on saddle armature with concave arc surface in small caliber railgun', *IEEE Trans. Plasma Sci.*, 2019, **47**, (5), pp. 2347–2353

[21] Ghassemi, M., Barsi, Y.M., Hamedi, M.H.: 'Analysis of force distribution acting upon the rails and the armature and prediction of velocity with time in an electromagnetic launcher with new method', *IEEE Trans. Magn.*, 2007, **43**, (1), pp. 132–136

[22] Musolino, A.: 'Finite-element method/method of moments formulation for the analysis of current distribution in rail launchers', *IEEE Trans. Magn.*, 2005, **41**, (1), pp. 387–392

[23] Tang, L.L., He, J.J., Chen, L.X., *et al.*: 'Current concentration of large-caliber C-shaped armature in square railgun', *IEEE Trans. Plasma Sci.*, 2015, **43**, (5), pp. 1125–1130

[24] Sousa, H., Oliveira, A., Xavier, G., *et al.*: 'Analysis of alternative parameters of dynamic resistance measurement in high voltage circuit breakers', *High Volt.*, 2019, **4**, pp. 197–202

[25] Glises, R., Baucour, P., Vaudrey, A., *et al.*: 'Electrothermal modelling of the railroads catenaries', *IET Electr. Syst. Transp.*, 2012, **2**, (3), pp. 110–118

[26] Dasara, S., Mishra, V.: 'Shielding measures of power transformer to mitigate stray loss and hot spot through coupled 3D FEA', *High Volt.*, 2017, **2**, pp. 267–273

[27] Andrade, A., Costa, E., Fernandes, J., *et al.*: 'Thermal behaviour analysis in a porcelain-housed ZnO surge arrester by computer simulations and thermography', *High Volt.*, 2019, **4**, pp. 173–177

[28] Lv, Q.A., Li, Z.Y., Lei, B., *et al.*: 'On velocity skin effect – part I: physical principle analysis and equivalent models' simulation'. 17th IEEE Int. Symp. on Electromagnetic Launch Technology, San Diego, USA, July 2014, pp. 1–7

[29] Marshall, R.A., Ying, W.: '*Railguns: their science and technology*' (China Machine Press, Beijing 2004, 1st edn.)

[30] Stankevič, T., Schneider, M., Balevičius, S.: 'Magnetic diffusion inside the rails of an electromagnetic launcher: experimental and numerical studies', *IEEE Trans. Plasma Sci.*, 2013, **41**, (10), pp. 2790–2795

[31] Ding, T., Chen, G.X., Bu, J., *et al.*: 'Effect of temperature and arc discharge on friction and wear behaviours of carbon strip/copper contact wire in pantograph–catenary systems', *Wear*, 2011, **271**, (9–10), pp. 1629–1636

[32] Wan, X.B., Lou, J.Y., Lu, J.Y., *et al.*: 'Thermal analysis in electromagnetic launcher with different section shape rails', *IEEE Trans. Plasma Sci.*, 2018, **46**, (6), pp. 2091–2098

[33] Bramerdorfer, G.: 'Tolerance analysis for electric machine design optimization: classification, modeling and evaluation, and example', *IEEE Trans. Magn.*, 2019, **55**, (8), pp. 1–9

[34] Xia, B., Hong, S., Choi, K., *et al.*: 'Optimal design of winding transposition of power transformer using adaptive co-kriging surrogate model', *IEEE Trans. Magn.*, 2017, **53**, (6), pp. 1–4

[35] Xiao, S., Liu, G.Q., Zhang, K.L., *et al.*: 'Multi-objective Pareto optimization of electromagnetic devices exploiting kriging with lipschitzian optimized expected improvement', *IEEE Trans. Magn.*, 2018, **54**, (3), pp. 1–4

[36] Xiao, S., Rotaru, M., Sykulski, J.K.: 'Adaptive weighted expected improvement with rewards approach in kriging assisted electromagnetic design', *IEEE Trans. Magn.*, 2013, **49**, (5), pp. 2057–2060

[37] Xiao, S., Zhang, K.L., Liu, G.Q., *et al.*: 'Multi-variable electromagnetic optimization design exploiting hybrid kriging', *IEEE Trans. Magn.*, 2017, **44**, (7), pp. 1837–1844